THE EFFECT OF NANO PORE SIZE AND POROSITY ON DEFORMATION BEHAVIORS OF ANODIC ALUMINUM OXIDE MEMBRANES

Jingyao Dai[1], Jogender Singh[2], Namiko Yamamoto[1]
Department of Aerospace Engineering, Pennsylvania State University[1]
Hammond Building 229
University Park PA 16803
Applied Research Laboratory, Pennsylvania State University[2]
4000D Applied Science Building
University Park PA 16803

ABSTRACT

With unique combination of properties such as low density, high strength, thermal stability and corrosion resistance, ceramics are essential for aerospace and other applications involving extreme environments. However, current application of ceramics is limited due to their low fracture toughness. In this study, the effects of nanoporosity on the mechanical deformation behaviors, particularly quasi-plasticity, were studied by conducting nanoindentation tests on anodic aluminum oxide (AAO) membranes. AAO membranes with varying porosity (~10-30%), pore diameter (~38-210 nm) and material phases (amorphous and polycrystalline) were tested using Berkovich and cube-corner tips under load up to ~400 mN. Measurement of apparent elastic modulus and hardness, combined with post-indentation SEM inspections, was performed on the AAO samples. Their mechanical behaviors were studied as a function of varying porosity, pore size and phase combinations. During nanoindentation using a cube-corner tip, shear bands in the form of collapsed or deformed pore arrays were observed around the indentation impressions, resulting in quasi-ductility when the samples have smaller pore size (~38-61 nm) or larger porosity (~20-30 %). This new failure mechanism induced by nanoporosity can potentially enhance ceramics' ability to dissipate energy and thus increase the fracture toughness. If such toughening is successful, such nanoporous ceramics can potentially be used in structural applications in extreme environments, including aero-engines, gas turbines, protection armors, thermal protection tiles and heat exchangers.

1. INTRODUCTION

Ceramic materials have a combination of properties including high strength and hardness, high thermal stability, high wear and corrosion resistance, low density, and low thermal and electrical conductivities [1]. Due to these properties, ceramics are desired in a wide range of applications including engine manufacturing, gas turbine, roller bearings, protection armor against high strain rate impact etc. [2]. However, the low damage tolerance of ceramics, which originate from the strong ionic and covalent bonding, currently limits their applications. Compared to other engineering materials, ceramics have comparable strength but much lower fracture toughness. Ceramics' fracture toughness is highly dependent on the distribution of defects and weak points in the materials, making the failure prediction difficult [3].

Due to the low damage tolerance of ceramics, a lot of applications that could benefit from using ceramic parts are still dominated by metal based materials such as various superalloys. In the past decades, multiple toughening methods have been developed and studied: transformation toughening [4,5], crack deflection toughening [6,7], fiber/whisker toughening [8,9], ductile phase toughening [10], etc. Progresses including the development of ceramic matrix composites (CMCs) have enabled the application of ceramic shrouds or even rotating blades in core sections of turbine engines [11]. With the development of nanotechnology including new characterization and manufacturing methods, new toughening methods for ceramics also start to show potential in further enhancement of their mechanical properties. Besides techniques such as toughening using carbon nanotubes [12,13] and graphene based materials [14] which utilizes existing toughening mechanism with novel materials, new toughening mechanisms enabled by the advancement of nanocrystalline ceramics have also emerged. In the recent work by K.M. Reddy et al. [15], nanocrystalline boron carbide (B_4C) ceramics with nanoporosity and amorphous carbon interface phases exhibit high damage tolerance (75 % higher toughness than microcrystalline B_4C) under indentation contact load. Porosity, which is traditionally regarded as a defect and leads to fracture, when reduced to nanometer size and accompanied by the soft grain boundary phases, eliminates under deformation and thus leads to enhanced plasticity and toughness. Similar mechanism was seen in the study by Z. Xia et al. on nanoporous aluminum oxide membranes [16] and their CNT composites [17]; nanopore collapse in shear bands instead of crack formation was observed around the indentation impression. This mechanism can potentially enhance the damage tolerance and toughness by reducing the stress concentration and by absorbing energy during the deformation process.

Despite the potential enhancement of damage tolerance that can be achieved through the introduction of nanoporosity, few studies have been conducted on this new deformation mechanism. In this study, we aim to parametrically study the effect of parameters such as pore size and porosity on the deformation behavior, more specifically the fracture behavior of nanoporous ceramics. Due to its highly ordered and controllable nanoporous structure, anodic aluminum oxide (AAO) membranes were chosen for this study. Nanoindentation was selected as the material characterization technique; the method only requires moderate sample preparation and can provide local material properties. Two different sharp indenter tips, Berkovich and cube-corner, were utilized in order to measure the material properties and to create different stress and deformation fields within the test samples. Since several parameters including pore size, porosity, and phase (crystalline vs. amorphous) can contribute to the toughening of nanoporous ceramic materials, mechanical properties (Young's modulus and hardness) were measured for multiple sets of samples while varying the above parameter combinations. Subsequent inspection of indented sample surface using scanning electron microscopy (SEM) further revealed the transition of deformation and fracture behavior as a function of the parameters.

2. EXPERIMENTATION

2.1 Sample preparation

Nanoporous AAO membranes can be manufactured using the standard two step anodization method [18] which yields highly organized, transverse isotropic porous and amorphous micro-structure. The AAO membranes of ~50 µm thickness were obtained from InRedox LLC. As manufactured, these AAO membranes have 10 % porosity and three different pore diameters (38 nm, 82 nm and 120 nm). A subsequent etching process was performed on these samples to enlarge

pores, and yielded higher porosity (~20-30%) while the inter-pore distances were maintained. The AAO samples with ~20 % porosity have the pore diameters of 50 nm, 119 nm, and 170 nm, and the AAO samples with ~30 % porosity have the pore diameters of 61 nm, 144 nm, and 210 nm. Since the AAO membranes were first grown on pure alumina substrates and later detached, the two surface sides, namely barrier layer and top, have slightly different pore diameter and surface morphology (see Figure 1a, 1b, and 1d). However, upon SEM inspection of the cross section of the samples (see Figure 1c), the pore diameter was mostly isotropic throughout the sample thickness.
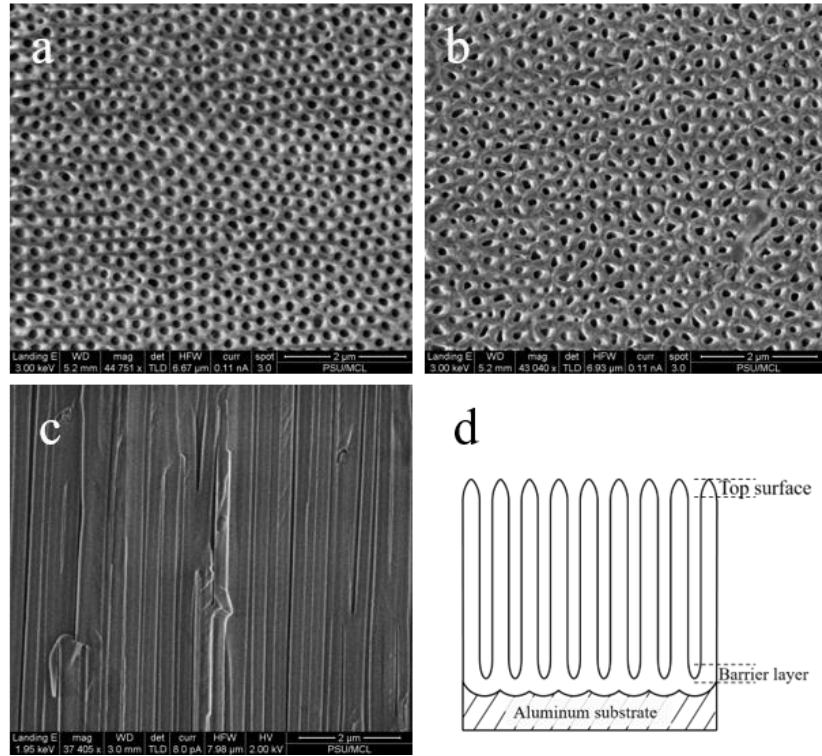

Figure 1. SEM images of (a) top surface (b) barrier layer surface (c) fractured cross section for a AAO sample with 119 nm pore size and 20 % porosity (d) a schematic of AAO on aluminum substrate.

The purchased AAO samples were amorphous in nature. Heat treatment was performed on some pristine amorphous samples to transform them to polycrystalline. A holding temperature of 900 ˚C was selected since amorphous alumina starts to transform into crystalline phases at temperatures above 800 ˚C [19]. A low heating and cooling rate of 1 ˚C per minute and a short holding time of 1 hour were selected to limit the warping of thin membranes. The entire process was carried out in a tube furnace with argon flowing through at around 50 cc/min. After the heat treatment, samples remained nondeformed. When inspected using SEM, the nanoporous structure of the AAO membranes were confirmed not altered by the heating process. Subsequent XRD tests confirmed the crystallinity (a mixture of γ, δ and θ phases) of the heat treated AAO samples.

2.2 Material Characterization

Mechanical properties of the AAO membranes with varying pore size (~38-210 nm), porosity (~10-30 %) and material phase (crystalline vs. amorphous) combination were evaluated through nanoindentation tests. The nanoindentation experiments were performed using a MTS Nanoindenter XP with continuous stiffness measurement (CMS) capability, maximum indentation load of 500 mN and 50 nN load resolution. Both Berkovich and cube-corner indenter tips were used in this study. The Berkovich tip was used mainly to measure the hardness (H) and elastic modulus (E). The cube-corner tip was used to initiate fracture within the samples at relatively lower load. A depth control loading method with 0.1 /s strain rate was selected with maximum indentation depth of 2 µm for the Berkovich tip and 4 µm for the cube-corner tip in consideration of the instrument's loading capacity and sample thickness. The AAO samples were first attached to stainless steel AFM sample mounting disks using super glue, then mounted onto the testing stage using wax. Calibration of tip area function for both Berkovich and cube-corner tips was performed beforehand on a piece of fused silica, mounted on the stage with the same process, with known and well defined elastic modulus and hardness. Indents at multiple indentation depths (0.4 µm, 0.8 µm, 1.2 µm, 1.6 µm, and 2.0 µm for the Berkovich tip and 1 µm, 2 µm, 3 µm, and 4 µm for the cube-corner tip) were performed and repeated for 4 to 5 times on each sample. Load and indentation depth data were collected. CMS measurement was also enabled to record the E and H data during the loading processes; an oscillation magnitude (harmonic displacement) of 2 nm and frequency of 45 Hz were used for CMS setting.

Analysis of nanoindentation test data was done using the standard Oliver and Pharr method [20]. The effective Young's modulus E can be calculated using the following equation:

$$\frac{1}{E_r} = \frac{(1-\nu^2)}{E} + \frac{(1-\nu_i^2)}{E_i} \tag{1}$$

Where E_i and ν_i (E_i: 1100 GPa, ν_i: 0.07) are the Young's modulus and Poisson's ratio of the diamond indenter tip. E and ν are the Young's modulus and Poisson's ratio of the sample. Here the Poisson's ratio of 0.2 was assumed for the samples for data analysis. E_r is the reduced elastic modulus which can be obtained from the unloading stiffness recorded during the indentation process through the following relation:

$$S = \frac{dP}{dh} = \frac{2}{\sqrt{\pi}} E_r \sqrt{A} \tag{2}$$

Here S is the experimentally measured unloading stiffness of the upper portion of the unloading curves, P is the indentation load, h the indentation depth of the tip and A is the projected area of the elastic contact which is calibrated and expressed as a polynomial with respect to indentation depth h. Using the contact area A along with the maximum indentation load P_{max}, the hardness H is defined as:

$$H = \frac{p_{max}}{A} \tag{3}$$

While being measured from the unloading curves, the Young's modulus and hardness data were constantly monitored during the loading process using the CSM method [21]. The data from

standard unloading curves were then averaged for further analysis; the data measured from loading curves using CMS were used to examine the existence of indentation size effect and to compare with the data from standard unloading curves. To examine the deformation behavior of nanoporous AAO membranes after the nanoindentation tests, SEM inspection was performed on a FEI NanoSEM 630 FESEM.

3. RESULTS AND DISCUSSIONS

3.1 Mechanical Properties

The E and H calculated from the equations (1-3) are summarized in Figure 2 and 3. The measured E and H (E: 100~120 GPa; H: 5~8 GPa) for the amorphous AAO samples with ~10 % porosity are in the same range when compared with values measured about amorphous AAO samples in the previous studies [16,24,25]. When compared with fully dense sintered polycrystalline alumina (E: ~340 GPa, H: ~15 GPa), the E and H values of these AAO membranes are much smaller due to the amorphous phase and nanoporous structure of the as-manufactured AAO membranes.

As seen in Figure 2, the elastic modulus E for both amorphous and crystalline AAO samples generally show the decreasing trend with increasing porosity. For example, with the sample set with small inter-pore distance (see Figure 2a and 2d), the elastic modulus, measured using a Berkovich tip, dropped from 99 GPa to 57 GPa for amorphous samples and from 109 GPa to 61 GPa for crystalline samples when the porosity is increased from 10% to 30%. This trend is consistent with previous studies [24,25]. The trend is also valid regardless of the sample surface side (top or barrier layer), but the measured E values showed difference depending on the surface side with polycrystalline samples with larger inter-pore distances (see Figure 2e and 2f). Some exception was observed with some samples: amorphous samples with larger inter-pore distance (see Figure 2c) and polycrystalline samples with medium inter-pore distance (see Figure 2e). These discrepancies are possibly caused by the non-homogeneity and poor consistency of porosity and pore size due to the etching process to enlarge pore size. Further inspection is needed to identify the cause of such phenomenon.

Testing results also show that the pore size and inter-pore distance affect the Young's modulus of the AAO membranes. For the crystalline AAO samples of the same porosity, E is measured to be higher with increasing pore size (see Figure 2d, 2e and 2f). For crystalline AAO samples with 10% porosity, the Young's modulus measured by cube-corner tip on barrier layer surface increased from 119 GPa to 186 GPa when pore size is increased from 38 nm to 210 nm. On the other hand, the measured E values of the amorphous AAO samples were mostly determined by the porosity, and were not largely affected by the pore size (see Figure 2a, 2b and 2c).
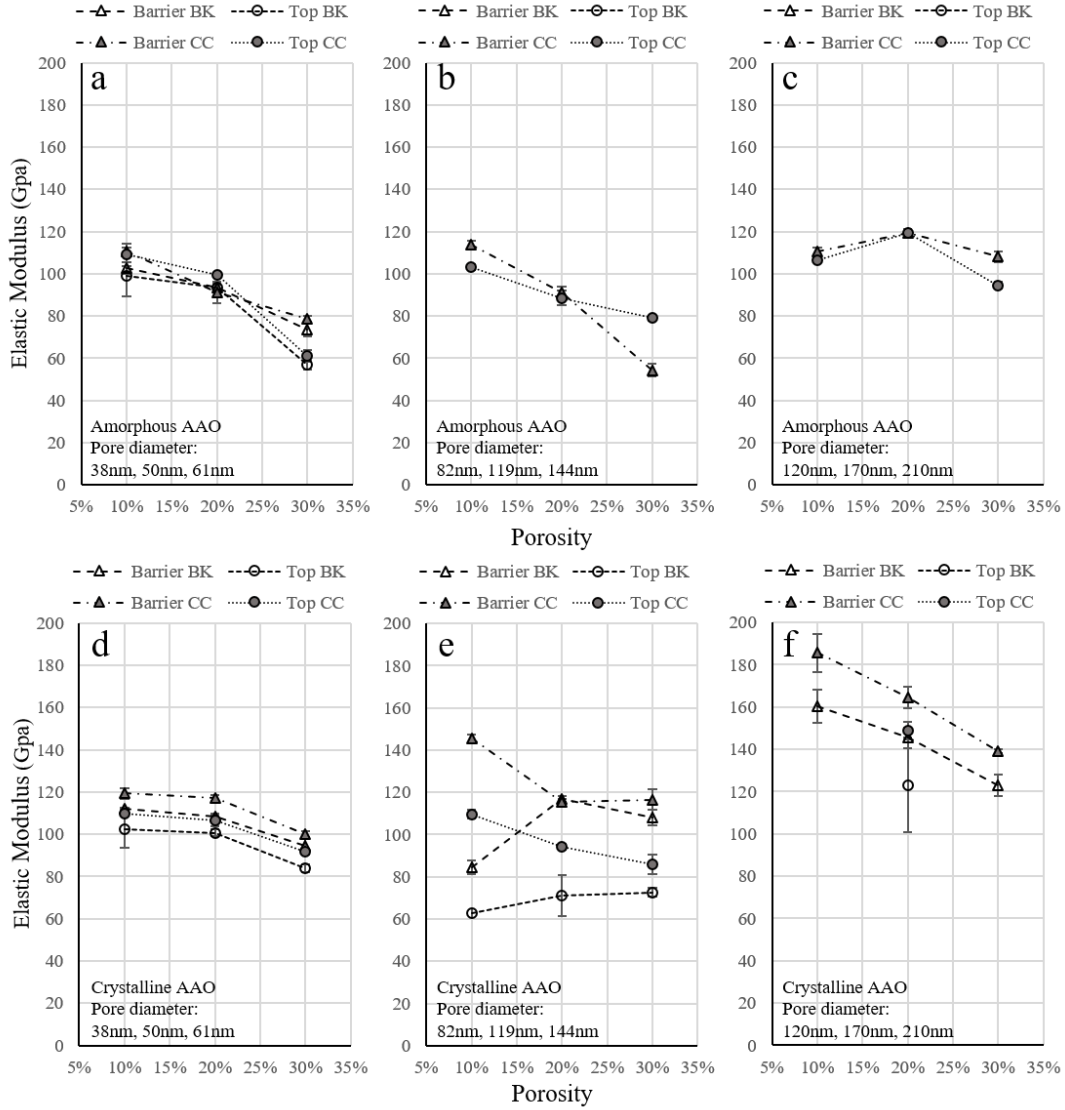
Figure 2. Elastic modulus of amorphous AAO (a), (b), (c) and crystalline AAO samples (d), (e) (f), with different pore size and porosity combinations by both berkovich and cube-corner indenter tips.

The trends of hardness with varying pore size, porosity, and phase were similar with those observed with Young's modulus, as summarized in Figure 3. For the AAO sample sets with the same inter-pore distance, the hardness decreases with increasing porosity. For example, the hardness values measured by indenting on the top surface of crystalline AAO with the smallest inter-pore distance decrease from 6.8 GPa to 5 GPa when porosity increases from 10 % to 30 % (see Figure 3d). Similar to the case for elastic modulus, increase of hardness value was seen among the crystalline AAO samples of the same porosity when pore size is increased (see Figure 3d, 3e and 3f). while only limited change of hardness values with respect to changing pore size for amorphous AAO was observed (see Figure 2a, 2b and 2c).
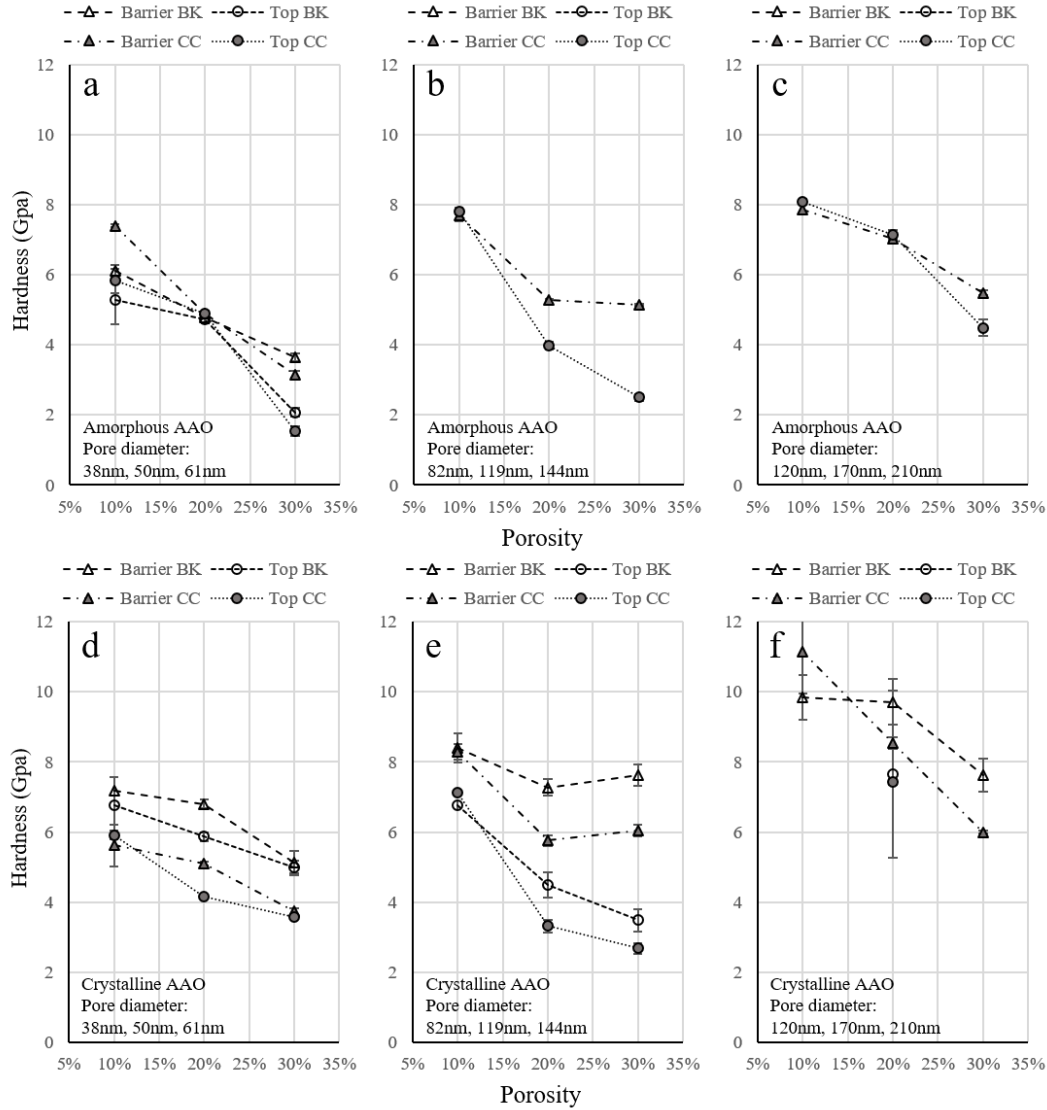
Figure 3. Hardness of amorphous AAO (a), (b), (c) and crystalline AAO samples (d), (e), (f) with different pore size and porosity combinations by both berkovich and cube-corner indenter tips.

The significant increase of elastic modulus values and hardness values for crystalline AAO with increasing pore size while porosity being maintained is likely due to the increase of grain size for heat treated AAO samples. We hypothesize that during the heat treatment process of pristine amorphous AAO samples, crystalline alumina grains start to nucleate and grow with their size restrained by the space between nanopores. With the same porosity, the AAO samples with larger pore size thus larger inter-pore distance yield larger grain size indicating a larger grain to grain boundary ratio than samples with smaller pore size. The crystalline AAO samples with larger pore size and grain size thus tend to behave more like bulk polycrystalline alumina with a higher elastic modulus and hardness. Meanwhile, the crystalline AAO samples with small pore size, with a lower grain to grain boundary ratio, behave more like amorphous AAO samples with a much lower value for elastic modulus and hardness. Amorphous AAO samples on the other hand exhibit no significant size effect.

3.2 Deformation Behaviors

The deformation behaviors of the AAO membranes after indentation were inspected using SEM. With a maximum indentation depth of 2 µm for Berkovich tip and 4 µm for cube-corner tip which correspond to a maximum indentation load of ~400 mN, radial cracks typical for sharp indenter tips can only be observed in a few samples with very short crack length. Instead of radial cracks, pore collapse in the form of shear bands extended from the edges of indentation impression similar to the ones in the work of Z. Xia et al [16,17] were observed.
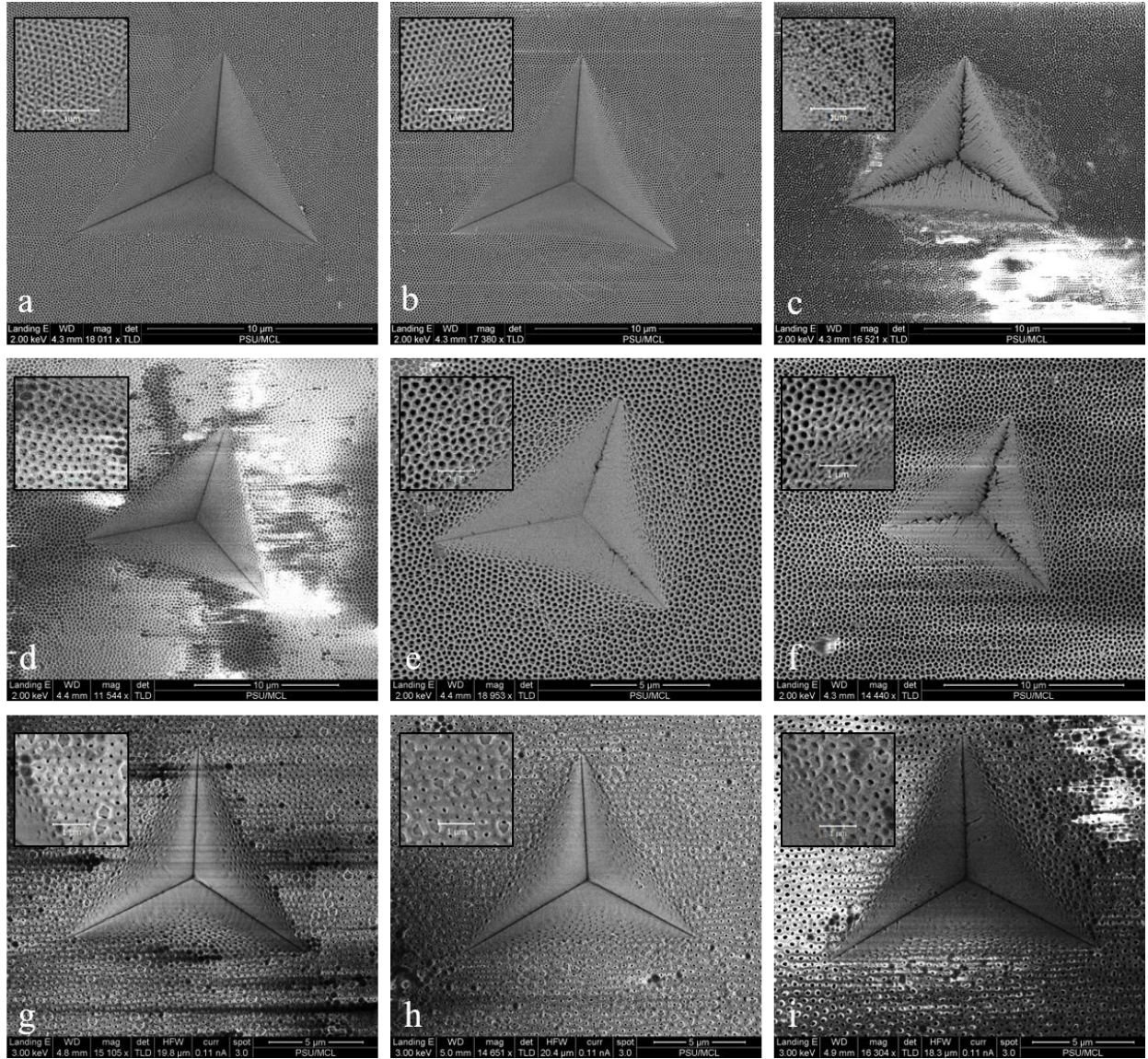

Figure 4. SEM images of indentation impression by cube-corner tip for amorphous AAO samples with different pore size and porosity: (a) 38 nm, 10 % (b) 50 nm, 20 % (c) 61 nm, 30 % (d) 82 nm, 10 % (e) 119 nm, 20 % (f) 144 nm, 30 % (g) 120 nm, 10 % (h) 170 nm, 20 % (i) 210 nm, 30%. The insertions show zoomed in images of porous microstructure around the indentation impression.

A transition of deformation behavior was observed with respect to both pore size and porosity. SEM images in Figure 4 are showing the top surfaces of the amorphous AAO samples indented with the cube-corner tip. The effect of porosity on the deformation behavior of AAO can be clearly seen in the sample set with the same inter-pore distance (Fig 4a, 4b, and 4c). With the same inter-pore distance, the sample with lower porosity (~10 %) shows no shear banding behavior while sample with moderate porosity (20 %) exhibits clear shear bands around the indented region. In Figure 4b, a series of shear cracks emerge between arrays of neighboring collapsed pores and extend outwards from the indentation impression center. With further increased porosity (~30 %, see Figure 4c), the indented surface shows a more localized pore collapse behavior; instead of the initiation of shear bands, the porous structure around the indentation impression and close to its edge appears to be crushed in a similar manner of yielding of honeycomb structure under compression [22].

The formation of shear bands seems to only happen for the samples with smaller pore sizes, when deformation behaviors were compared among samples with the same porosity and different pore size. For samples with the same 20 % porosity (Fig 4. (b), (e), (h)), shear bands can be clearly observed in AAO with small pore diameter of 50 nm. With the pore size increased to 119 nm, the pore collapse still happen, but in a more random manner where no clear shear bands formed by arrays of collapsed pores can be identified. For sample with large pore size 170 nm, only limited nanocracks between pores can be seen around the indentation impression.
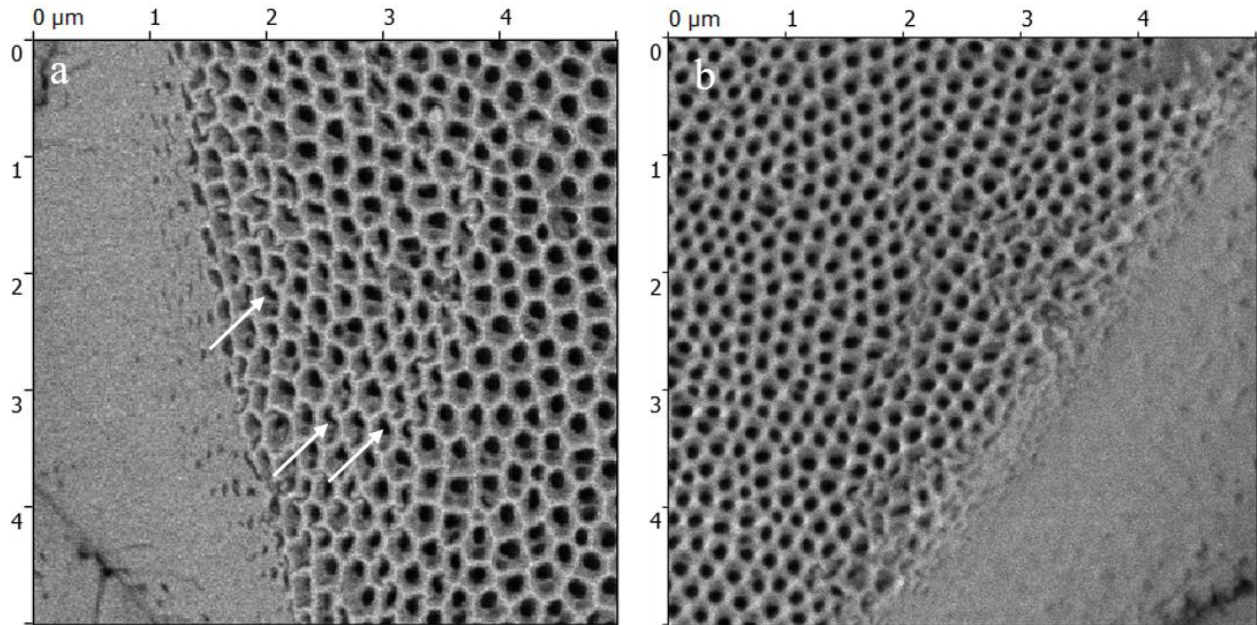

Figure 5. SEM images of deformed porous structure for (a) amorphous AAO with 119 nm pore size and 20 % porosity (b) crystalline AAO with 119 nm pore size and 20 % porosity.

The pore collapse mechanisms of the amorphous and crystalline AAO samples are compared in Figure 5. Inspection of the crystalline AAO samples indented with a cube-corner tip generally shows similar shear banding and deformation transition with respect to pore size and porosity as the ones observed with the amorphous AAO samples. However, closer inspection of collapsed pore structure indicates difference in the deformation mechanism. In Figure 5a, the nanoporous

structures around the indentation impression of the amorphous AAO sample not only fracture but also go under plastic deformation where the edges of originally hexagonal shaped pore structures got bended and sheared. Pore structures for the crystalline AAO sample in Figure 5 (b), on the other hand, show no sign of such plastic deformation behavior with nanocracks forming in a more brittle manner.
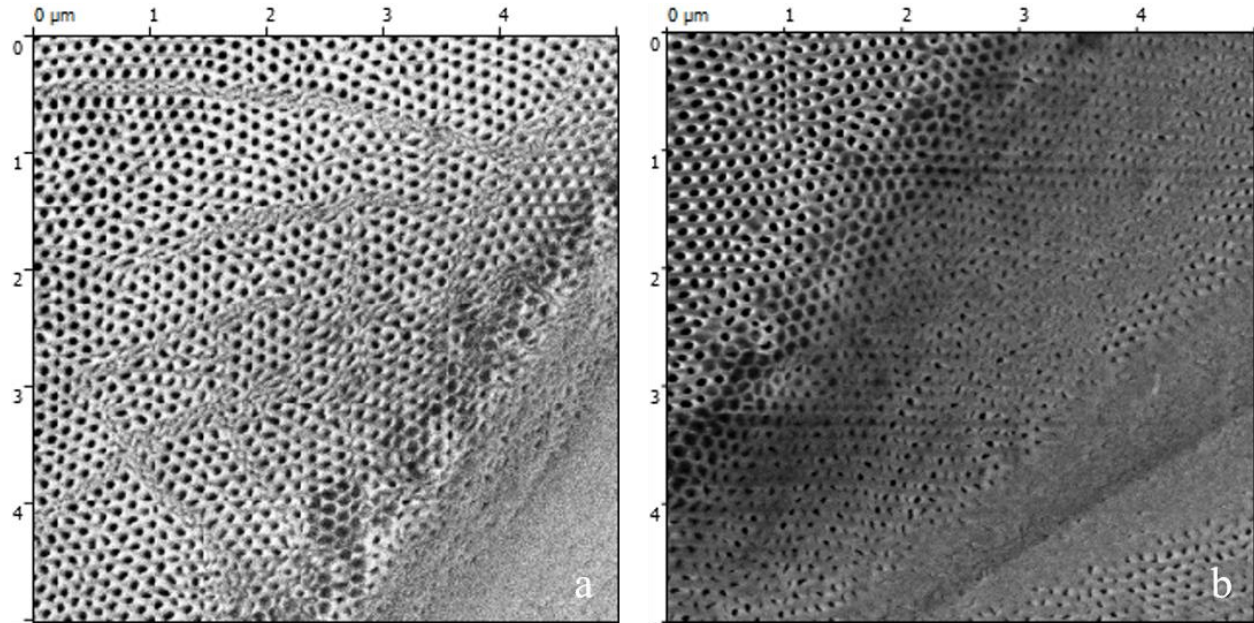

Figure 6. SEM images of deformed porous structure for crystalline AAO with 61nm pore diameter and 30% porosity indented using (a) Cube-corner tip (b) Berkovich tip.

Besides the material phase, we observed that the change in loading condition could also contribute to difference in deformation behaviors. Mechanical deformation using different indenters are compared in Figure 6. Shear bands were seen around the indented area extending away from the center of the indentation impression made with the cube-corner tip. For the samples with the same pore size, porosity and material phase indented by the Berkovich tip, arrays of collapsed pores parallel to the indentation impression edge and inside the impression was observed.

4. CONCLUSIONS

In this study, the effects of nano pore size, porosity, and phase on the mechanical properties and deformation behaviors of AAO membranes were studied using nanoindentation.

For mechanical properties, both elastic modulus (E) and hardness (H) decrease with increasing porosity due to the change in volume fraction of material under indentation. A clear size effect can only be observed for crystalline AAO samples where elastic modulus and hardness increase with increasing pore size or inter-pore distance for the same porosity. This unique trend can be attributed to the larger grain size thus higher volume ratio of grain to grain boundary in crystalline AAO samples with larger pore size. With larger grains and less grain boundary phases, the AAO samples behave in a similar manner as bulk crystalline alumina. Samples with small grains and more grain boundary phases behave more like amorphous AAO samples.

For deformation behaviors, shear banding was observed for the AAO samples with small pore size (~38 nm-61 nm) or moderate/high porosity (~ 20-30 %). A transition from shear bands formed by arrays of collapsed pores to localized pore collapse in a more random manner was observed when porosity is increased from 10 % to 30 %. When inter-pore distance and pore size are increased however, the shear banding behavior becomes less significant with limited pore collapse around indentation impression for the same porosity. Comparison between the amorphous and polycrystalline AAO membranes also revealed the more brittle behavior of heat treated polycrystalline AAO samples.

Future work includes processing of indentation test data using energy method, mechanical testing, measurement of fracture toughness for AAO samples using methods other than nanoindentation. These tasks will be conducted in order to further understand the shear banding behavior of AAO which could potentially enhance the damage tolerance of ceramic materials.

5. REFERENCES

1. Barsoum, Michel, W. *Fundamentals of Ceramics*. London: Institute of Physics Publishing, 2003

2. Boch, P., Niepce, J. C. *Ceramic Materials: Processes, Properties and Applications*. Hoboken NJ: John Wiley & Sons, 2010

3. Munz, D., Fett, T. *Ceramics: Mechanical Properties, Failure Behaviour, Materials Selection*. New York NY: Springer Berlin Heidelberg New York, 1999

4. Hannink, R. H. J., Kelly, P. M., Muddle, B.C. "Transformation toughening in zirconia-containing ceramics." *Journal of the American Ceramic Society* 83(3) (2000): 461-487

5. Garvie, R. C., Hannink, R. H., Pascoe, R. T. "Ceramic Steel." *Nature* 258(5537) (1975): 703-704

6. Steinbrech, R. W. "Toughening mechanisms for ceramic materials." *Journal of the European Ceramic Society* 10 (1992): 131-142

7. Gilbert, C. J., Cao, J. J., De Jonghe, L. C., Ritchie, R. O. "Crack-growth resistance-curve behavior in silicon carbide: Small versus long cracks." *Journal of the American Ceramic Society* 80(9) (1997): 2253-2261

8. Naslain, R. R. "SiC-matrix composites: Nonbrittle ceramics for thermos-structural application." *International Journal of Applied Ceramic Technology* 2(2) (2005): 75-84

9. Evans, A.G. "Perspective on the Development of High-Toughness Ceramics." *Journal of the American Ceramic Society* 73 (1990): 187-206

10. Sigl, L. S., Mataga, P. A., Dalgleish, B. J., McMeeking, R. M. "On the Toughness of Brittle Materials Reinforced with a Ductile Phase." *Acta Metallurgica* 36(4) (1988): 945-953

11. Zok, F. W. "Ceramic-matrix composites enable revolutionary gains in turbine engine efficiency." *American Ceramic Society Bulletin* 95 (2016): 22-28

12. Zhan, G. D., Kuntz, J. D., Wan, J., Mukherjee, A. K. "Single-wall carbon nanotubes as attractive toughening agents in alumina-based nanocomposites." *Nature Materials* 2(1) (2003): 38-42

13. Ma, R. Z., Wu, J., Wei, B. Q., Liang, J., Wu, D. H. "Processing and properties of carbon nanotubes-nano-SiC ceramic." *Journal of Materials Science* 33(21) (1998): 5243-5246

14. Walker, L. S., Marotto, V. R., Rafiee, M. A., Koratkar, N., Corral, E.L. "Toughening in graphene ceramic composites." *ACS Nano* 5(4) (2011): 3182-3190

15. Reddy, K. M., Guo, J. J., Shinoda, Y., Fujita, T., Hirata, A., Singh, J. P., McCauley, J. W., Chen, M. W. "Enhanced mechanical properties of nanocrystalline boron carbide by nanoporosity and interface phases." *Nature Communications* 3 (2012): 1052

16. Xia, Z., Riester, L., Sheldon, B. W., Curtin, W. A., Liang, J., Yin, A., Xu, J. M. "Mechanical properties of highly ordered nanoporous anodic alumina membranes." *Reviews on Advanced Materials Science* 6(2) (2004): 131-139

17. Xia, Z., Riester, L., Curtin, W. A., Li, H., Sheldon, B. W., Liang, J., Chang, B., Xu, J. M. "Direct observation of toughening mechanisms in carbon nanotube ceramic matrix composites." *Acta Materialia* 52(4) (2004): 931-944

18. Masuda, H., Fukuda, K. "Ordered metal nanohole arrays made by a two-step replication of honeycomb structures of anodic alumina." *Science* 268(5216) (1995): 1466

19. McQuaig, M. K., Toro, A., Van Geertruyden, W., Misiolek, W. Z. "The effect of high temperature heat treatment on the structure and properties of anodic aluminum oxide." *Journal of Materials Science* 46 (2011): 243-253

20. Oliver, W. C., Pharr, G. M. "An improved technique for determining hardness and elastic modulus using load and displacement sensing indentation experiments." *Journal of Materials Research* 7(06) (1992): 1564-1583

21. Li, X. D., Bhushan, B. "A review of nanoindentation continuous stiffness measurement technique and its applications." *Materials Characterization* 48(1) (2002): 11-36

22. Parka, S. D., Kyriakides, S. "In-Plane Compressive Response and Crushing of Honeycomb." *Journal of the Mechanics and Physics of Solids* 42(10) (1994): 1499-1532

23. Coble, R. L., & Kingery, W. D. "Effect of porosity on physical properties of sintered alumina." *Journal of the American Ceramic Society* 39(11) (1956): 377-385

24. Vojkuvka, L., Santos, A., Pallarès, J., Ferré-Borrull, J., Marsal, L. F., & Celis, J. P. "On the mechanical properties of nanoporous anodized alumina by nanoindentation and sliding tests." *Surface and Coatings Technology* 206(8) (2012): 2115-2124

25. Tsyntsaru, N., Kavas, B., Sort, J., Urgen, M., & Celis, J. P. "Mechanical and frictional behavior of nano-porous anodized aluminium." *Materials Chemistry and Physics* 148(3) (2014): 887-895